

Novel 3D-Flower Shaped KTaO₃ Nanostructures: A Perovskite with Highly Efficient Photocatalytic and H₂ Generation Ability

Praveen B M (✉ bm.praveen@yahoo.co.in)

Srinivas University

Sumedha H N

Srinivas University

Shashank M

Kuvempu University

Sergio R. Teixeira

Federal University of Rio Grande do Sul

Nagaraju G

Siddaganga Institute of Technology

Article

Keywords: Areca seed powder, KTaO₃, Flower structure, Rose Bengal, H₂ generation

Posted Date: March 16th, 2022

DOI: <https://doi.org/10.21203/rs.3.rs-1425864/v1>

License:   This work is licensed under a Creative Commons Attribution 4.0 International License.

[Read Full License](#)

Abstract

Treatment of industrial wastewater is one of the biggest challenges that mankind is facing today to prevent environmental pollution and its associated adverse effects on human health. Environmentalists across the world have given a clarion call for dye degradation, wastewater treatment and their effective management in our surrounding habitats. Despite significant progress in the development of new water treatment technologies, new materials haven't matured enough for large scale industrial applications. Hence, the development of new scalable and sustainable multifunctional materials having the potential to treat wastewater and generate energy is the need of the hour. In this direction, novel 3D-flower shaped KTaO_3 (3D-F-KT) material has been synthesized using areca seed powder as a green fuel. This new material has been successfully applied for the treatment of industrial wastewater contaminated with Rose Bengal. The efficiency of the material was analysed using several parameters like catalytic loading, dye concentration, kinetic and scavenging experiments, photostability and recyclability. In addition, the material was subjected to optical studies and H_2 generation, making it a highly versatile multifunctional material, exhibiting a degradation efficiency of 94% in a short span of 150 minutes and a photocatalytic H_2 generation efficiency of 374 mmol g^{-1} through water splitting. With an immense potential, KTaO_3 presents itself as a multifunctional catalyst that can be scaled up for a variety of industrial applications ranging from wastewater treatment to energy generation and storage.

Highlights

- KTaO_3 was synthesized using novel areca seed powder as a green fuel.
- Photocatalytic degradation and hydrogen generation were tested at different concentration of the fuel.
- A dye degradation efficiency of 94% was achieved.
- The rate of photocatalytic H_2 generation was found to be 374 mmol g^{-1} .

1. Introduction

One of the major sources of water pollution is the rejected wastes from textile industries. The dissolved dye stuffs in water bodies can cause serious problems to aquatic animals and human life, in addition to various chemical and biological changes that occur during the utilisation of dissolved oxygen¹. At present, textile wastes are being cleaned using various chemical, biological and physical processes. Conventional techniques like sedimentation, oxidation by chemical methods, filtration and coagulations have many drawbacks due to the formation of various byproducts, and the associated energy and cost intensive methods^{2,3}. Hence, nanoparticles with high photocatalytic properties are being explored as a solution to eliminate harmful pollutants from water bodies. Semiconductor-based metal oxide nanoparticles (MNPs) are capable of removing organic pollutants from wastewater streams and exhibit

good catalytic activity⁴⁻⁶. The higher catalytic activity is due to the interaction of light rays (photon) and the catalyst that yields CO₂ and H₂O⁷⁻⁹.

Over the past few years, tantalates have garnered significant research interest because of their potential in a wide range of applications e.g., wastewater treatment, air adsorbents, energy storage, production of hydrogen, etc. Perovskite structures of tantalates such as NaTaO₃, KTaO₃, and LiTaO₃ have been recently reported to exhibit good photocatalytic property. In particular, potassium tantalate (KTaO₃) is an outstanding material on account of its excellent dielectric properties and perovskite cubic structure at all temperatures. The conduction band with the Ta (5d) orbital observed at higher negative position is one of the reasons for its excellent behaviour during photocatalytic reactions^{10,11}. Such photocatalysts also tend to possess abilities to act as electrocatalysts in the generation of hydrogen through the process of water splitting, which is known as green hydrogen. Among the renewable and non-renewable sources of energy, hydrogen production via renewable processes is perceived as one of the cleanest forms of energy, as the non-renewable fuel sources pose significant challenges in terms of sustainability and environmental impact. The surge in the energy requirements across the globe has created a need to find cost-effective alternatives to the currently used expensive catalysts such as platinum (Pt) and iridium (Ir). In this direction, the use of solar energy to obtain pure hydrogen from water with the help of photoelectrochemical and photocatalytic processes have attracted significant interest [7]. Production of hydrogen by splitting water using sunlight is a promising way to convert solar energy into chemical energy. This type of conversion is more sustainable compared to other processes as it needs only water, catalyst and light. Therefore, choosing a convenient photocatalyst that degrades pollutants in water and also exhibits superior water splitting abilities is crucial and highly essential.^{7,12,13}. To this effect, the photocatalytic performance of perovskite alkali metal tantalates (NaTaO₃, KTaO₃) has been studied in detail and different approaches of their preparation have been examined. These materials are abundant, non-toxic and have a higher negative conduction band edge than the H⁺/H₂ energy levels¹⁴⁻¹⁶. Here, we have synthesised KTaO₃ by combustion method using areca seed as a green fuel, and analyzed the structural and morphological characteristics of the synthesised material using various analytical, spectroscopic and microscopic techniques. In addition, the kinetics, mechanism of photodegradation, and water splitting ability of the material for the generation of hydrogen have been reported in detail, providing new dimensions for the development of such novel materials and extension of their applications beyond wastewater treatment.

2. Materials And Methods

2.1 Preparation of Areca Seed Powder

Areca seeds were sourced from an agricultural area in Sringeri, Chikmagalur District, Karnataka, India. The plant material was initially washed with distilled water several times and dried in shade for 2-3 days. The obtained dried seeds were powdered into uniform sized particles using an electric mixer (Philips Mixer Grinder, 750W) and were stored at room temperature until further use.

2.2 Synthesis Method

3D flower-like KTaO_3 (3D-F-KT) nanostructures were prepared by an eco-friendly green combustion process using areca seed powder as the fuel. Tantalum (V) oxide (Ta_2O_5) and potassium hydroxide (KOH) were procured from Sigma Aldrich (AR) and used without any further purification. 0.4 g each of Ta_2O_5 and areca seed powder were mixed thoroughly and ground in an agate mortar for 15 minutes. The obtained mixture was added to a crucible containing 1.4 M KOH solution and was stirred for 15 minutes. The crucible was kept in a pre-heated muffle furnace at 500 ± 10 °C for nearly 10 minutes and was later calcined at 700 °C for 4 hours in static air. A fine milky white powder was finally obtained. The synthesis of 3D-F-KT nanostructures was repeated with different concentrations of areca seed such as 0.2 and 0.8 g respectively. The obtained product was stored in an air tight container for further use.

2.3 Characterization

The particle size and morphological features were studied using scanning electron microscopy (Neo-Scope JCM-6000PLUS system) and transmission electron microscopy (JEOL- JEM 2100). The phase purity and crystal structure were determined by the X-ray diffraction patterns and were acquired using Rigaku Smartlab X-ray diffractometer (Cu-K α , $\lambda = 1.5406$ Å) operating at 40 kV and 30 mA. The infrared spectrum was recorded using a Fourier Transform Infrared Spectrometer (Bruker Alpha P) in the range of 400 to 4000 cm^{-1} . The photoluminescence (PL) of the samples were recorded with an Agilent Technology-Cary-60 and their optical properties were analysed using LABINDIA technologies UV 3092 spectrophotometer. The specific surface area and pore size of the catalyst was studied using Quanta Chrome Nova 2200E - BET Surface Area Analyser.

3. Results And Discussions

3.1 Powder X-ray Diffraction (P-XRD)

Figure 1 shows the XRD patterns of the 3D-F-KT nanostructures synthesized using areca seed powder with different concentrations (0.2, 0.4, 0.8 g). All the peaks (100), (110), (111), (200), (210), (211), (220), (300), (310), (311), (222), (320) match well with the JCPDS Card No.38-1470 having lattice constants of $a = b = c = 3.9883$ Å, $\alpha = \beta = \gamma = 90^\circ$, space group = Pm-3m and space group number = 221. The average crystallite size of 3D-F-KT nanostructures (0.2, 0.4, 0.8 g of areca seed powder concentration) was calculated using the following Debye-Scherrer's equation and was found to be 29.07, 26.89, and 33.12 nm respectively.

$$D = \frac{K\lambda}{\beta \cos\theta}$$

Where K is the crystallite shape constant (0.89), λ is the wavelength of X-ray Cu-K α radiation (1.5406 Å), β is the Full width at half maximum (FWHM) and θ is the glancing angle. The strong and narrow width of the peaks indicates the high purity and crystallinity of 3D-F-KT nanostructures. Therefore, from the above data it can be inferred that the fuel (areca seed powder) could be responsible for the variation in particle sizes of 3D-F-KT nanostructures^{17,18}.

3.2 Diffuse Reflectance Spectra (UV-DRS)

The diffuse reflectance spectrum was used to observe the band gap of 3D-F-KT nanostructures, which displayed an intense band at 420 nm, indicating the absorption of the host lattice. It can be clearly seen that the addition of more than 50 wt% of the fuel significantly affects the optical absorption properties of 3D-F-KT nanostructures and exhibits an enhanced visible light absorption towards the longer wavelength. Hence, to determine the band gap (E_g), Kubelka-Munk (K-M) theory was adopted from the diffuse reflectance spectra. The tangent interception of the $[F(R)_\infty/h\nu]^{1/2}$ plots versus photon energy ($h\nu$) has been shown in Figs. 2a and 2b. The photon energy ($h\nu$) and Kubelka – Munk function $F(R_\infty)$ were calculated using the following equations.

$$F(R_\infty) = \frac{(1 - R_g)}{2R_g}$$

2

$$h = \frac{1240}{\lambda}$$

3

where R_∞ is the reflection coefficient and λ is the absorption wavelength. The energy gap was found to be ~ 2.99 eV for the 3D-F-KT material.

3.3 Fourier Transform Infrared Spectra (FTIR)

FTIR spectra of 3D-F-KT nanostructures were recorded from 400-4000 cm^{-1} as shown in Fig. 3. An intense broad peak of Ta-O was observed at 609 cm^{-1} for the three different concentrations (i.e., 0.2, 0.4, 0.8 g) of 3D-F-KT nanostructures synthesized using areca seed powder. It was clearly observed that the carbon content present in the prepared material corresponds to the C=C vibration of the aromatic ring at 1653 cm^{-1} and the hydroxyl C-OH bending vibration can be attributed to the 1381 cm^{-1} . Further, by increasing the concentration of carbon in the 0.8 g sample, another peak at 1131 cm^{-1} was witnessed, that correlates to the C-O stretching vibrations or C-O-C epoxy vibrations. It can also be noticed that all the samples exhibited a broad peak at 3400 cm^{-1} due to the vibration of OH group and adsorption of water¹⁹.

3.4 Scanning Electron Microscopy (SEM)

The morphology of the 3D-F-KT nanostructures was studied using a scanning electron microscope (Neo-Scope JCM-6000PLUS system) and their representative images are shown in Fig. 4. As observed from the SEM images, the synthesized material KTaO_3 has a well-developed flower like 3D structure with different sizes. It is the first time that flower-shaped 3D- KTaO_3 nanostructures were synthesised by combustion method and are being reported.

3.5 Transmission Electron Microscope (TEM)

The TEM (JEOL- JEM 2100 system) images of the nanostructures are shown in Figs. 5a and 5b. The d-spacing value was found to be 0.38 nm as shown in Fig. 5(c). This matches well with the (100) plane obtained from the XRD analysis. Fig. 5 (d) shows the SAED pattern with 2 bright fringes and corresponds to the XRD planes (100) and (110).

3.6 Brunauer-Emmett-Teller Surface Area Studies

To investigate the surface area and pore volume of the 3D-F-KT nanostructures, Brunauer–Emmett–Teller technique was used, and the associated N_2 adsorption-desorption isotherm studies were carried out at 77 K (Fig. 6). A clear type-IV isotherm curve indicates the mesoporous nature of the material with an average pore diameter of 3.10 nm. Similarly, the specific surface area and pore volume were found to be $3.74 \text{ m}^2\text{g}^{-1}$ and $0.009 \text{ cm}^3\text{g}^{-1}$ respectively. The surface area has also contributed significantly to the enhanced photocatalytic activity of the 3D-F-KT nanostructures.

3.7 Photocatalytic Degradation

The photocatalytic activity of 3D-F-KT nanostructures with different concentration (0.2, 0.4, 0.8 g) was examined using rose bengal dye in the presence of visible light irradiation ($\lambda > 420 \text{ nm}$) and a schematic representation depicting the process has been shown in Scheme 1. Initially, to observe the degradation efficiency in the absence of visible light, photolysis was conducted in a dark condition. After 30 minutes of the reaction time, no degradation was observed. Later, the experiment was carried out by collecting the reaction mixture for every 30 minutes to check the rate of dye degradation. As it can be observed from Fig. 7(a), 0.4 g of the fuel concentration showed an appreciable degradation efficiency (>90%) compared to other fuel concentrations. A comparative analyse of the degradation property of KTaO_3 nanostructures with different dyes and pollutants were made and their data is given in Table 1.

Table-1

Literature survey with Degradation of different pollutants by KTaO_3 and its composites.

Material	Source of light	Dye	% of degradation	Time (min)	Ref.
30 wt% rGO-KTaO ₃	Visible	Phenol	43	60	19
0.5Au/1.5Pt-KTaO ₃	Visible	Phenol	14.75	90	25
2.0 Rh-KTaO ₃	Visible	Toluene	41.98	60	25
KTaO ₃ +CdS+MoS ₂ (10:5:1)	LED	Toluene	60	60	26
KTaO ₃	LED	Toluene	64	60	26
KTaO ₃ -CdS(10:1)	UV-Vis	Phenol	59	60	26
54wt%BiOI/KTaO ₃	Visible	Rhodamine B	98.6	30	27
N-KTaO ₃	Visible	Methylene blue	98.3	240	28
KTaO ₃	Visible	Rose bengal	94	150	Present work

3.7.1 Effect of Catalytic Load

It is well-known that the amount of photocatalyst significantly affects the degradation rate of dyes. Hence, to find out the optimum catalytic load, different amounts of the catalyst (10, 20, 30, 40 mg) were used with rose bengal dye at pH 7. The effect of different amounts of the photocatalyst (KTaO₃ nanostructures) on the degradation rate has been shown in Fig. 7(b). Upon increasing the catalytic load, the degradation rate also increased up to a certain amount and thereafter, no effect was observed. This may be due to the fact that as the amount of photocatalyst increased, the number of active sites available on the surface of KTaO₃ nanostructures also increases with an increase in the exposed surface area. However, after a certain weight i.e., 40 mg, there was no increase in the specific surface area and hence, the active sites. This was considered to be the saturation point, above which not much of photocatalytic degradation was observed, as adding the photocatalyst beyond this point would allow it to settle at the bottom of the tube. Further, the formation of turbidity in the reaction mass indicates the fall of degradation rate. Therefore, the optimum weight of the photocatalyst for the effective degradation of rose bengal dye was found to be 40 mg.

3.7.2 Effect of Dye Concentration

Fig. 7(c) shows the effect of different concentrations of rose bengal dye on the photocatalytic performance of 3D-F-KT nanostructures. With a fixed catalytic load of 40 mg at neutral pH, the

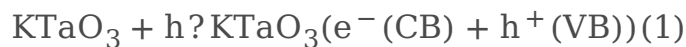
concentration of rose bengal dye was varied in terms of 5, 10, 15, 20 ppm per 100 ml of the reaction mixture. It was concluded that the photodegradation efficiency of rose bengal dye was inversely proportional to its concentration, which means that when the dye concentration was more, its photocatalytic degradation rate decreased at a fixed amount of catalyst. This may be attributed to the fact that the dye itself acts as an obstacle for the intensity of incident light and thus, affects the path length of the incoming light. Hence, it can be concluded that at 5 ppm dye concentration, a degradation efficiency of 90% was observed.

3.7.3 Effect of pH

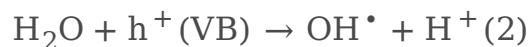
As shown in Fig. 7(d), pH plays an important role in varying the rate of photocatalytic degradation of dyes. The effect of pH on the degradation of rose bengal was studied by keeping the amount of catalyst and the dye concentration constant. In a solution having pH 3, the surface of the photocatalyst and the dye molecules become positively charged so that the dye molecule and the catalyst will repel each other. Thus, the catalytic reaction on the surface of the material takes place towards the smaller extent. Whereas a gradual decrease in the degradation rate was observed in alkaline solutions. This is due to the electrostatic repulsion between the negatively charged surface of the catalyst and the anionic rose bengal dye. So, the optimum pH value for the excellent degradation of rose bengal was found to be pH 5²⁰.

3.7.4 Mechanism of Dye Degradation

The generation of electrons in the conduction band and holes in the valence band takes place when the semiconductor nanostructures absorb light energy from an external source. The possible mechanism is shown below in Eq. (1).



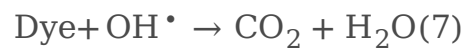
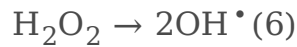
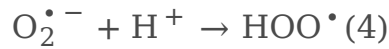
Water reacts with the generated holes at the valence band to give OH[•] which is a powerful oxidising agent to attack the nearest dye molecule as shown in Eq. (2).



Later, oxygen reacts with the generated electrons at the conduction band to give an anionic superoxide radical (O₂^{•-})



The recombination of the electron and the hole was thus reduced by the formation of a superoxide ion on 3D-F-KT surface and thus, maintains the neutrality of electrons. The generated $O_2^{\bullet -}$ is protonated to produce H_2O_2 and therefore, the OH^{\bullet} radical remains at last. Finally, the conversion of the hazardous dye (RB) into CO_2 and water takes place efficiently (4–7).



3.7.5 Kinetics of Photocatalytic Degradation

The kinetic study was carried out using Langmuir-Hinshelwood model for the rose bengal dye over 3D-F-KT nanostructures. The straight line obtained from the kinetic model indicates the dye removal over $KTaO_3$ and follows a pseudo-first-order kinetics as shown in Fig. 8. The observed slope value (k) from the plot was found to be $2.8 \times 10^{-2} \text{ min}^{-1}$ by using the formula $\ln(C_0/C_t) = kt$, where C_0 represents the initial concentration of the dye at $t=0$ and C_t is related to the final concentration after every 30 minutes.

3.7.6 Scavenging Experiments

The process of photocatalysis under visible light irradiation was examined using scavenging experiments by trapping the active species produced at the time of reaction. Here, tertiary-butyl alcohol (TBA) and potassium dichromate ($K_2Cr_2O_7$) were used as the scavengers for OH^{\bullet} and e^- respectively, while ascorbic acid (AA) and ethylenediaminetetraacetic acid (EDTA) were adopted as the scavengers for $O_2^{\bullet -}$ and h^+ respectively. Fig. 9 represents the degradation efficiency of rose bengal dye using 40 mg of 3D-F-KT without adding any scavengers. Apparently, the percentage degradation of the rose bengal dye did not exhibit much change after the addition of $K_2Cr_2O_7$ and EDTA, which implies that e^- and h^+ played a negligible role in the degradation process. However, with the addition of TBA or AA, the degradation rate of the rose bengal dye reduced, and only 67.86% or 73.13% degraded after 120 minutes of the reaction. The obtained result shows that OH^{\bullet} was the primary reactive species in the photocatalytic degradation of the rose bengal dye.

3.7.7 Recycling Experiment

The reusability and photostability of 3D-F-KT nanostructures were analysed using recycling experiments under the irradiation of visible light for 5 cycles as shown in Fig. 10(a). The photoreaction mixture was collected after every cycle, followed by centrifugation and filtration. The collected residue was washed with distilled water and was later recovered. The recovered material residue was reused for the subsequent degradation experiment as earlier. The degradation efficiency of the rose bengal dye decreased from 94% to 80% for the 1st and 5th cycles respectively. However, a loss in efficiency of only 14% was observed even after the 5th cycle, which shows that KTaO₃ nanostructures had an excellent photostability. Meanwhile, Fig. 10(b) represents the XRD spectrum of 3D-F-KT nanostructures before and after the degradation process. However, no differences in the peaks were found and the structure of the material appeared to be stable even after the degradation of the rose bengal dye.

3.7.8 Detection of Hydroxyl Radicals

The rate of formation of OH radicals can be found by a simple and effective photoluminescence (PL) technique by taking Coumarin as an investigator. During the degradation process, OH radicals are the most important reactants; it reacts with the coumarin molecule to produce 7-hydroxyl coumarin. In this study, 50 mg of 3D-F-KT nanostructures was dispersed in 100 ml of aqueous 0.5 mM coumarin and were air bubbled for 15 mins to understand the adsorption-desorption equilibrium in the dark condition. Furthermore, 300 W tungsten light source was used as an illuminator. 5 mL of the reaction mixture was drawn at every 30 mins to measure the photoluminescence spectrum using the Agilent Technologies Cary Eclipse-60 Spectrophotometer. From Fig. 11, it is evident that the intensity of the peaks in the PL spectra was directly proportional to the time of reaction. This provides stronger evidence to show the formation of OH radicals on the surface of the photocatalyst. Later, the OH radical production increases with time.

3.8 Photoluminescence Studies

The recombination efficiency of the photogenerated free charge carriers can be predicted by photoluminescence studies (PL). At room temperature, the emission and excitation spectrum of 3D-F-KT nanostructures were recorded and are shown in Fig. 12(a & b). The emission peak of 491 nm was observed at an excitation wavelength of 330 nm^{19,21}. The samples prepared by adding 0.2 and 0.4 g of the fuel showed lower PL intensities as compared to 0.8 g of the sample. This could lead to the fact that, more intensity of the emission peak indicates a higher recombination of the photogenerated electron and hole pairs, and therefore, lesser is the photocatalytic activity. It can also be seen that nanostructures synthesised using 0.2 and 0.4 g of the fuel gave almost similar photoluminescence peaks and were found have the most efficient separation of charge carriers. The colour of the emission spectra is shown in Fig. 12(c) and it is clear that the electrons jumped from the conduction band to the valence band by losing some amount of energy and hence, a higher emission wavelength at 491 nm and a lower excitation at 330 nm was observed. Meanwhile, it can be concluded that the emission of blue colour at 491 nm is as per the Commission International de l'Eclairage (CIE) 1931 chromaticity diagram²¹.

3.9 Photocatalytic H₂ Generation

The photocatalytic H₂ generation of the synthesised 3D-F-KT nanostructures was analysed using a 400 W Xenon lamp (UV-Vis light source). If the energy of the conduction band was negative compared to the reduction potential value H⁺/H₂ (0 V Vs NHE), and the energy of the valence band has a higher positive value than the oxidation potential O₂/H₂O (1.23 V Vs NHE), then the photocatalyst should satisfy the condition for water splitting. On irradiating the energy higher than the band gap energy of KTaO₃ photocatalyst, the excitation of electrons from valence to conduction band occurs by leaving holes in the lower energy level. To avoid the electron-hole recombination, the sacrificial agent consumes the produced holes from the valence band and thereby, results in an increased H₂ production. The factors for the photocatalyst to show good hydrogen generation are crystallinity, band gap, thickness of pore wall, particle size, hydrophilic group on the catalyst surface and the surface area. As depicted in Fig. 14, the hydrogen generation of 3D-F-KT (0.4 g concentration of areca seed powder) photocatalyst was found to be 374 μmolg⁻¹ for 5 hours. The photocatalytic activity of this material was based on factors like crystallinity, surface area, particle size, thickness of pore wall, number of hydrophilic groups on the catalyst surface and also the existence of active sites²². The schematic representation of the photocatalytic H₂ generation is given in Fig. 13. Moreover, 3D-F-KT nanostructures with 0.4 g fuel shows a higher H₂ generation value than the other two samples (0.2 and 0.8 g). Here, the higher H₂ generation was due to the more hydroxyl groups on the surface of the material^{23,24}.

4. Conclusion

The multifunctional property of potassium tantalate is the key factor behind its large application in various fields. In this way, we have successfully prepared novel 3D-F-KT nanostructures using areca seed powder as a green fuel by combustion method. All 3D-F-KT samples with different fuel ratios show an excellent photocatalytic activity under the irradiation of visible light. The prepared material shows an excellent degradation efficiency of up to 94% in a short time under visible light irradiation and also appreciable amount of H₂ is generated with a good potential of material. In addition, the photoluminescence (PL) studies proved that there was very less recombination of charge carriers during the reaction. The recycling experiment also shows the excellent durability of the photocatalyst. Finally, by observing the obtained results, it can be inferred that KTaO₃ can be adopted as a promising and an efficient material for both wastewater treatment and H₂ generation.

Declarations

Acknowledgements

Sumedha H N thanks to Centre of Applied Research and Nanotechnology (CARN) for providing SEM facility and Siddaganga Institute of Technology for their continuous support and encouragement. And

thanks to DST Nanomission (SR/NM/NS-1262/2013) and DST SERB (SB/FT/CS-083/2012) Govt. of India, New Delhi for financial support to procure XRD and UV-Visible spectrophotometer.

References

1. Wang, Z. *et al.* Overall water splitting by Ta₃N₅ nanorod single crystals grown on the edges of KTaO₃ particles. *Nature Catalysis* **1**, 756-763, doi:10.1038/s41929-018-0134-1 (2018).
2. Chen, Y., Xiang, Z., Wang, D., Kang, J. & Qi, H. Effective photocatalytic degradation and physical adsorption of methylene blue using cellulose/GO/TiO₂ hydrogels. *RSC Advances* **10**, 23936-23943, doi:10.1039/D0RA04509H (2020).
3. Borthakur, S. *et al.* Sunlight assisted degradation of a pollutant dye in water by a WO₃@g-C₃N₄ nanocomposite catalyst. *New Journal of Chemistry* **44**, 2947-2960, doi:10.1039/C9NJ05142B (2020).
4. Ashraf, W., Bansal, S., Singh, V., Barman, S. & Khanuja, M. BiOCl/WS₂ hybrid nanosheet (2D/2D) heterojunctions for visible-light-driven photocatalytic degradation of organic/inorganic water pollutants. *RSC Advances* **10**, 25073-25088, doi:10.1039/D0RA02916E (2020).
5. Chatterjee, M. J., Ghosh, A., Mondal, A. & Banerjee, D. Polyaniline–single walled carbon nanotube composite – a photocatalyst to degrade rose bengal and methyl orange dyes under visible-light illumination. *RSC Advances* **7**, 36403-36415, doi:10.1039/C7RA03855K (2017).
6. Bhattacharjee, A. & Ahmaruzzaman, M. Photocatalytic-degradation and reduction of organic compounds using SnO₂ quantum dots (via a green route) under direct sunlight. *RSC Advances* **5**, 66122-66133, doi:10.1039/C5RA07578E (2015).
7. Mahmoodi, N. M. Photocatalytic Degradation of Dyes Using Carbon Nanotube and Titania Nanoparticle. *Water, Air, & Soil Pollution* **224**, 1612, doi:10.1007/s11270-013-1612-3 (2013).
8. Rosy, A. & Kalpana, G. Influence of

RGO/TiO₂

RGO/TiO₂nanocomposite on photo-degrading Rhodamine B and Rose Bengal dye pollutants. *Bulletin of Materials Science* **41**, 83, doi:10.1007/s12034-018-1598-y (2018).
9. Jyothi, D., Deshpande, P. A., Venugopal, B. R., Chandrasekaran, S. & Madras, G. Transition metal oxide loaded MCM catalysts for photocatalytic degradation of dyes. *Journal of Chemical Sciences* **124**, 385-393, doi:10.1007/s12039-011-0148-6 (2012).
10. Achilleos, D. S., Kasap, H. & Reisner, E. Photocatalytic hydrogen generation coupled to pollutant utilisation using carbon dots produced from biomass. *Green Chemistry* **22**, 2831-2839, doi:10.1039/D0GC00318B (2020).
11. Wang, Q. *et al.* Photocatalytic hydrogen generation on low-bandgap black zirconia (ZrO₂) produced by high-pressure torsion. *Journal of Materials Chemistry A* **8**, 3643-3650, doi:10.1039/C9TA11839J (2020).

12. Shudo, Y.*et al.* Reduced graphene oxide-transition metal hybrids for hydrogen generation by photocatalytic water splitting. *Journal of Inclusion Phenomena and Macrocyclic Chemistry* **94**, 283-286, doi:10.1007/s10847-018-0795-z (2019).
13. Jhansi Rani, S. & Sathish Mohan, B. ZnS/Fe₂O₃/Ag Ternary Nanocomposite Photocatalyst for the Degradation of Dyes Under Visible Light. *Russian Journal of Physical Chemistry A* **94**, 392-400, doi:10.1134/S0036024420020144 (2020).
14. Ameen, S., Park, D.-R. & Shin, H. S. Silicon nanowires arrays for visible light driven photocatalytic degradation of rose bengal dye. *Journal of Materials Science: Materials in Electronics* **27**, 10460-10467, doi:10.1007/s10854-016-5135-8 (2016).
15. Chen, Z.*et al.* Synthesis of carbon doped KTaO₃ and its enhanced performance in photocatalytic H₂ generation. *Catalysis Communications* **109**, 6-9, doi:https://doi.org/10.1016/j.catcom.2018.02.006 (2018).
16. Hagiwara, H., Ono, N., Inoue, T., Matsumoto, H. & Ishihara, T. Dye-Sensitizer Effects on a Pt/KTa(Zr)O₃ Catalyst for the Photocatalytic Splitting of Water. *Angewandte Chemie International Edition* **45**, 1420-1422, doi:10.1002/anie.200503316 (2006).
17. Chang, S.*et al.* In-Situ Growth of Au on KTaO₃ Sub-Micron Cubes via Wet Chemical Approach for Enhanced Photodegradation of p-Nitrophenol. *Materials (Basel)* **12**, 1950, doi:10.3390/ma12121950 (2019).
18. Tong, L.*et al.* Normal and abnormal dielectric relaxation behavior in KTaO₃ ceramics. *RSC Advances* **7**, 50680-50687, doi:10.1039/C7RA09866A (2017).
19. Bajorowicz, B.*et al.* Perovskite-type KTaO₃-reduced graphene oxide hybrid with improved visible light photocatalytic activity. *RSC Advances* **5**, 91315-91325, doi:10.1039/C5RA18124K (2015).
20. Kaur, J. & Singhal, S. Heterogeneous photocatalytic degradation of rose bengal: Effect of operational parameters. *Physica B: Condensed Matter* **450**, 49-53, doi:https://doi.org/10.1016/j.physb.2014.05.069 (2014).
21. Zou, Y., Hu, Y., Gu, H. & Wang, Y. Optical properties of octahedral KTaO₃ nanocrystalline. *Materials Chemistry and Physics* **115**, 151-153, doi:https://doi.org/10.1016/j.matchemphys.2008.11.041 (2009).
22. Grewe, T. & Tüysüz, H. Designing Photocatalysts for Hydrogen Evolution: Are Complex Preparation Strategies Necessary to Produce Active Catalysts? *ChemSusChem* **8**, 3084-3091, doi:10.1002/cssc.201500774 (2015).
23. Chen, X., Shen, S., Guo, L. & Mao, S. S. Semiconductor-based Photocatalytic Hydrogen Generation. *Chemical Reviews* **110**, 6503-6570, doi:10.1021/cr1001645 (2010).
24. Xu, D.*et al.* Ag-Decorated ATaO₃ (A = K, Na) Nanocube Plasmonic Photocatalysts with Enhanced Photocatalytic Water-Splitting Properties. *Langmuir* **31**, 9694-9699, doi:10.1021/acs.langmuir.5b01294 (2015).
25. Krukowska, A.*et al.* Mono- and bimetallic nanoparticles decorated KTaO₃ photocatalysts with improved Vis and UV-Vis light activity. *Applied Surface Science* **441**, 993-1011,

doi:<https://doi.org/10.1016/j.apsusc.2018.02.077> (2018).

26. Bajorowicz, B., Cybula, A., Winiarski, M. J., Klimczuk, T. & Zaleska, A. Surface Properties and Photocatalytic Activity of KTaO₃, CdS, MoS₂ Semiconductors and Their Binary and Ternary Semiconductor Composites. *Molecules* **19**, 15339-15360 (2014).
27. Lu, X.*et al.* Fabrication of a novel BiOI/KTaO₃ p–n heterostructure with enhanced photocatalytic performance under visible-light irradiation. *RSC Advances* **10**, 10921-10931, doi:10.1039/C9RA10231K (2020).
28. Rao, M. P.*et al.* Synthesis of N-doped potassium tantalate perovskite material for environmental applications. *Journal of Solid State Chemistry* **258**, 647-655, doi:<https://doi.org/10.1016/j.jssc.2017.11.031> (2018).

Scheme

Scheme 1 is available in the Supplementary Files section.

Figures

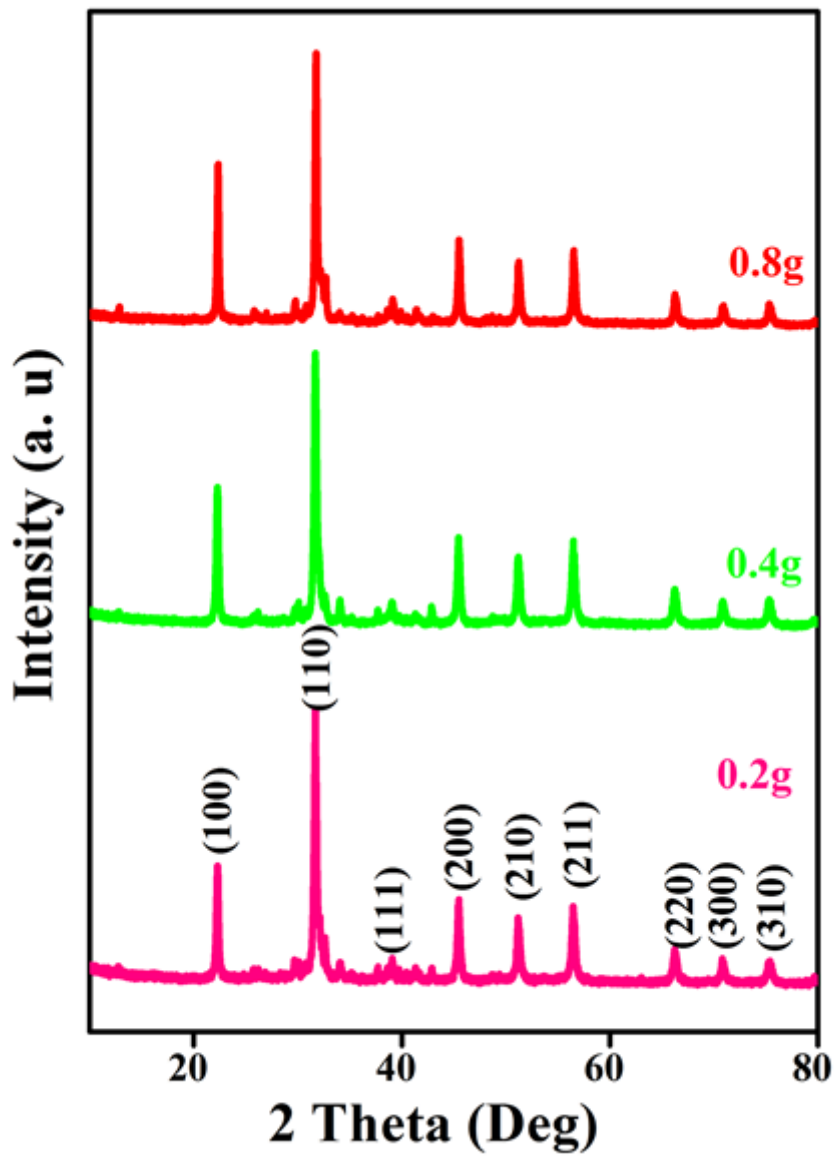


Figure 1

Intense XRD peaks of 3D-F-KT NPs prepared by 0.2, 0.4, 0.8g concentration of areca seed powder

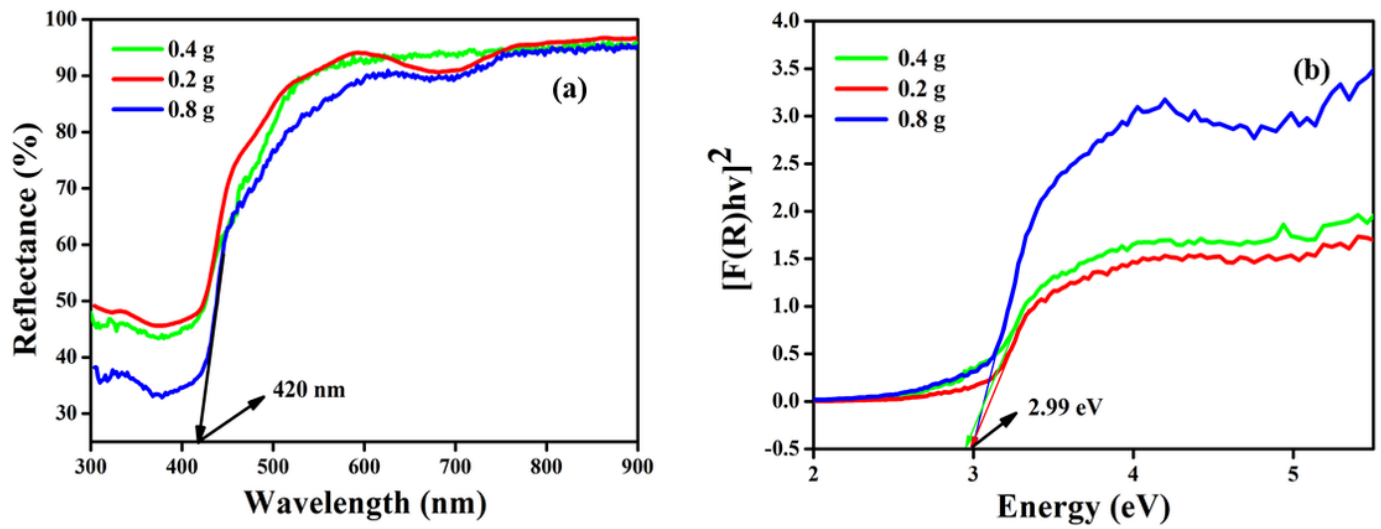


Figure 2

(a) Diffuse reflectance spectra showing absorbance towards visible region on increasing areca fuel weight of 3D-F-KT. (b) Controlled Direct band gap energy (E_g) of 3D-F-KT NPs achieved by increasing fuel ratio.

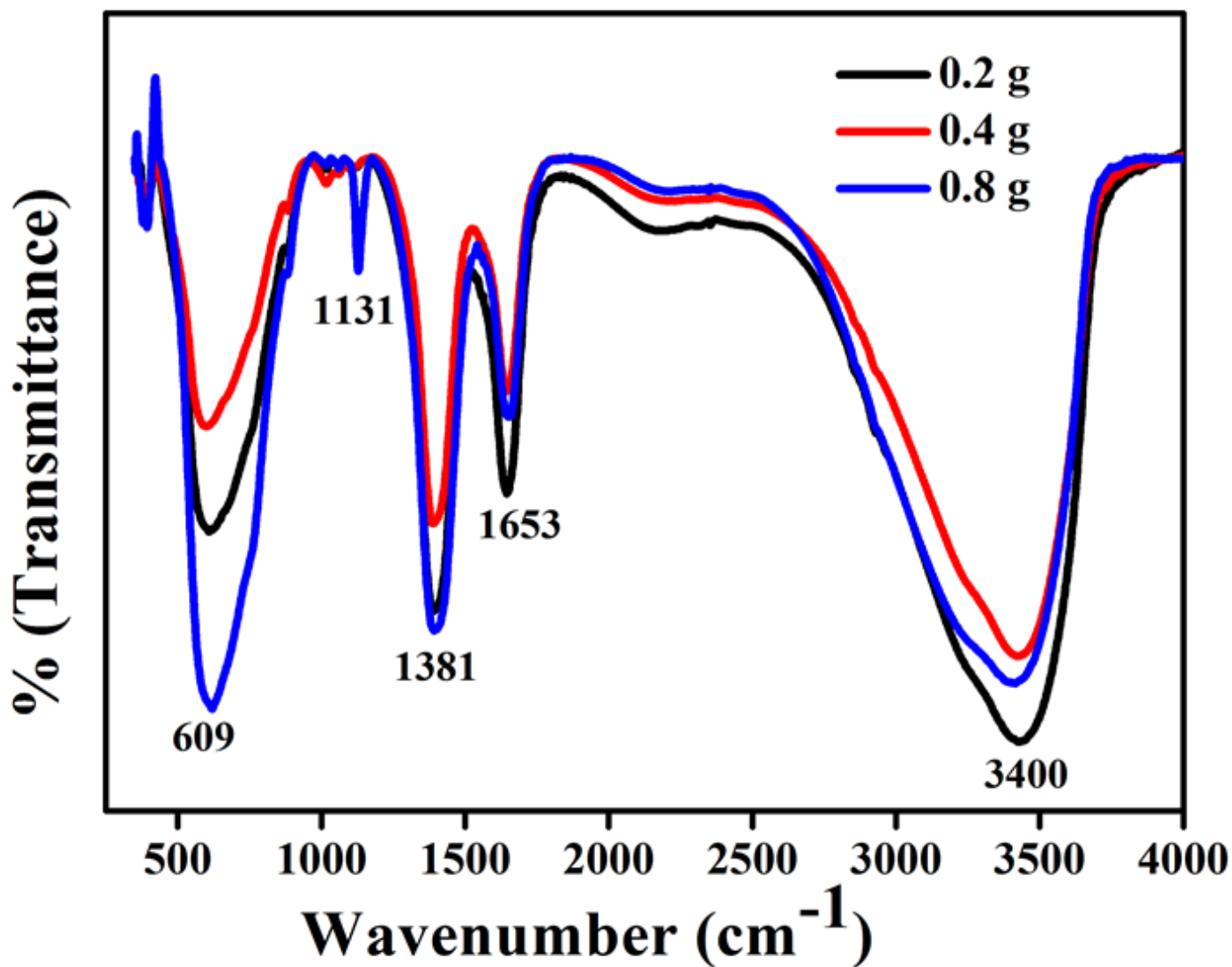


Figure 3

FTIR spectra of 3D-F-KT NPs showing intense Ta-O linkage (609 cm^{-1}) along with C=C vibration (1653 cm^{-1}) and alcoholic C-OH bending (1381 cm^{-1}). Another peak at 1131 cm^{-1} is due to C-O stretching, which is caused by adding excess amount of areca seed powder

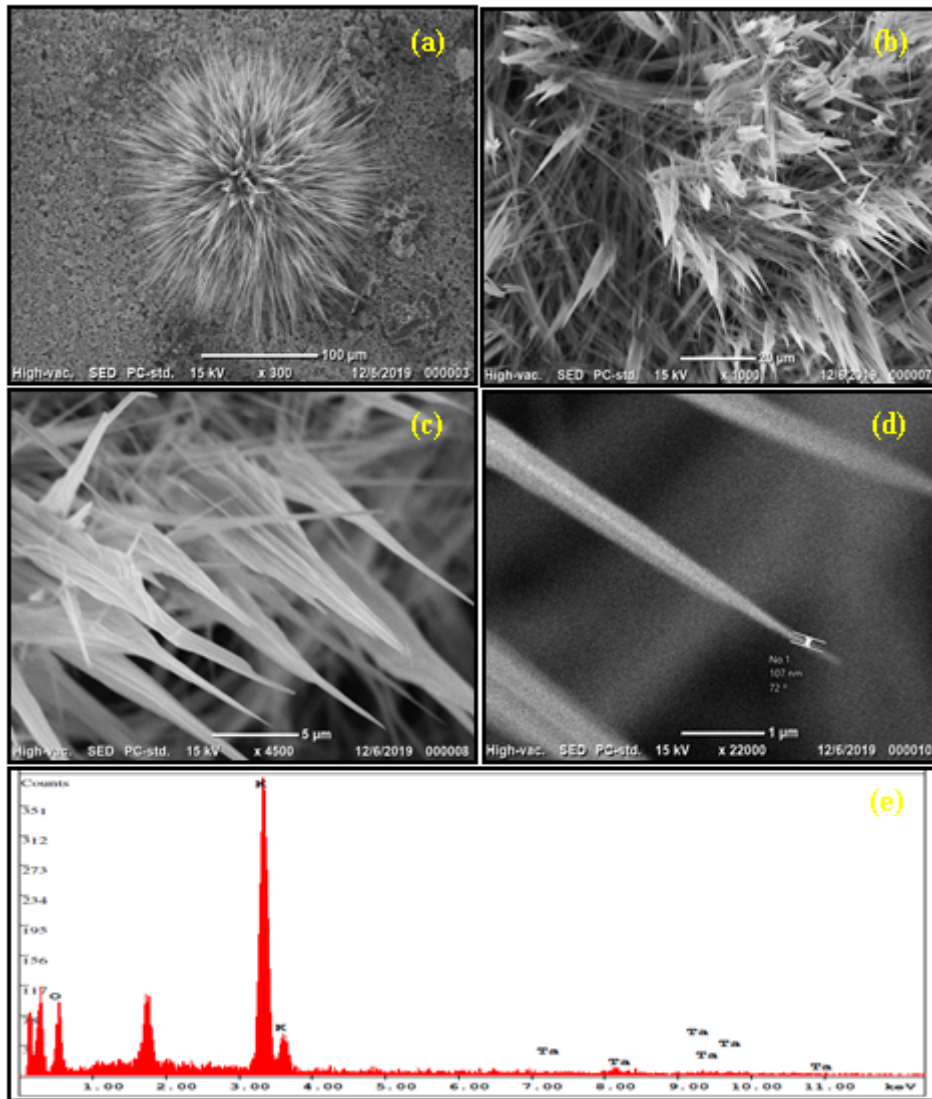


Figure 4

(a) 3D flowerlike structure observed at 100 μm range (b-c) Bunch of flower petals showing sharp edges (c) A needle embedded within single petal recorded at 1 μm range s of (0.4g concentration of areca seed powder)

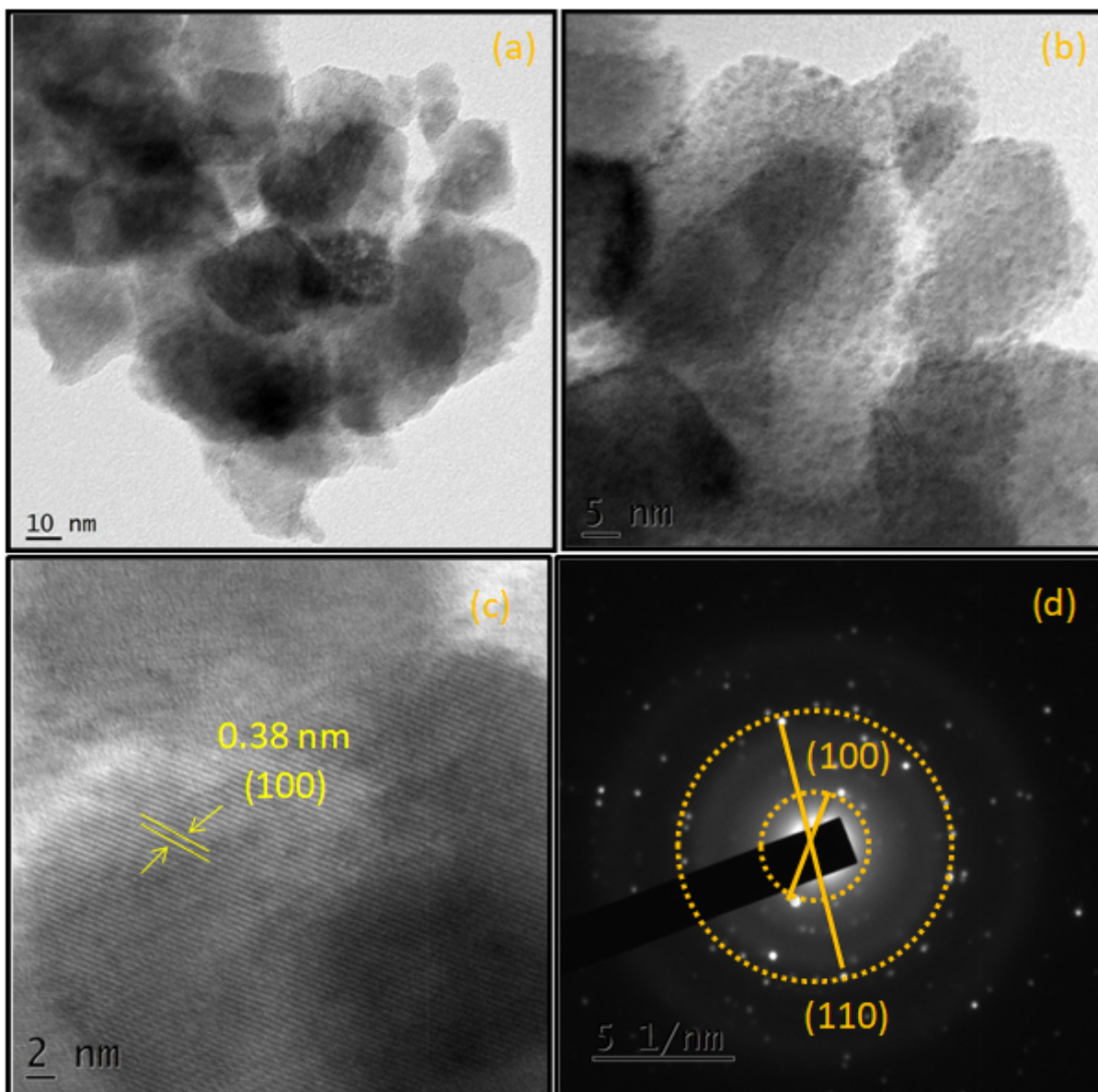


Figure 5

(a and b) TEM images with different magnifications (c) d-spacing value well matched with 100 XRD plane (d) SAED pattern showing 2 bright fringes of 3D-F-KT NPs (0.4g concentration of areca seed powder)

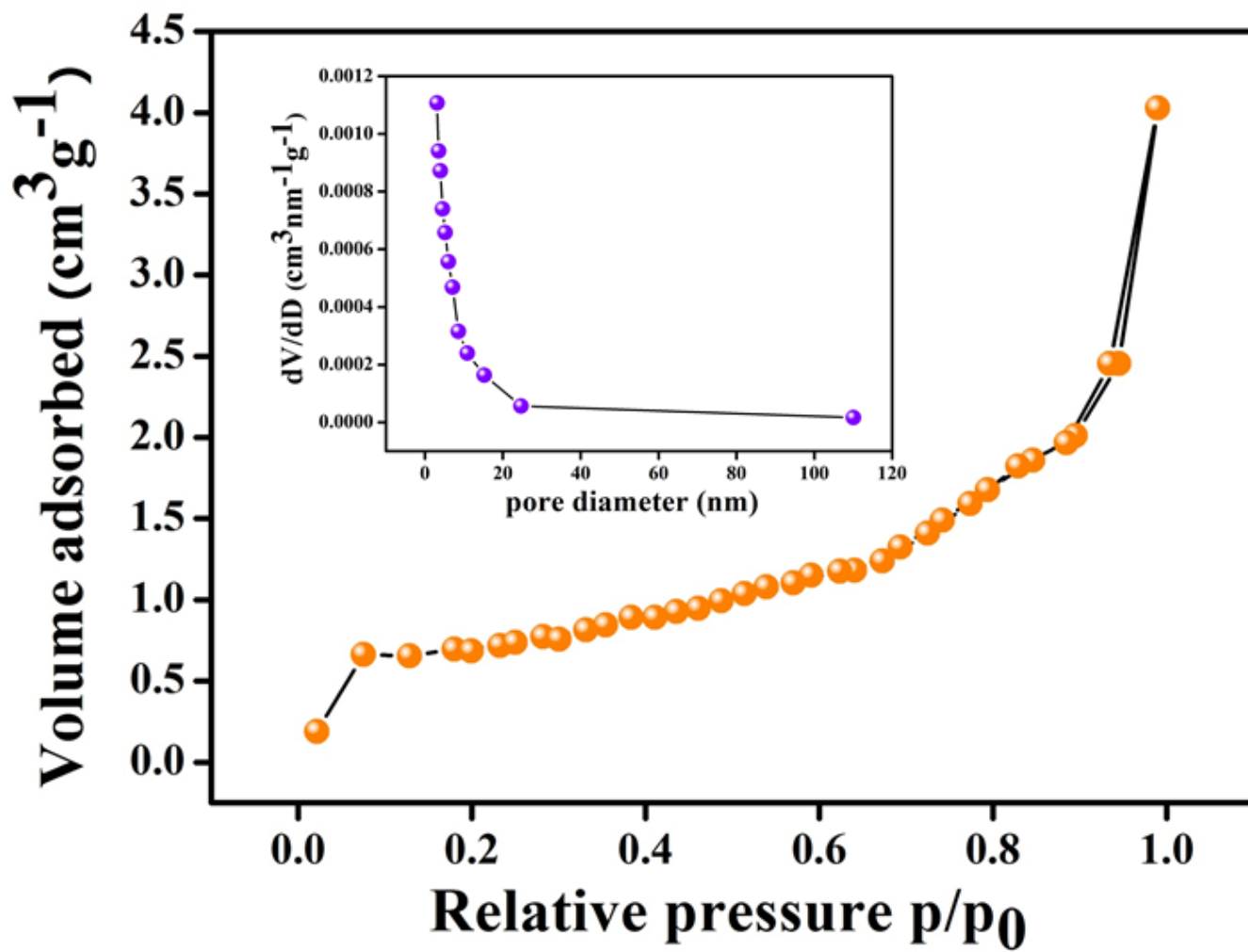


Figure 6

BET specific surface area, pore volume and average pore diameter of 3D-F-KT NPs (Inset: Pore diameter measurements)

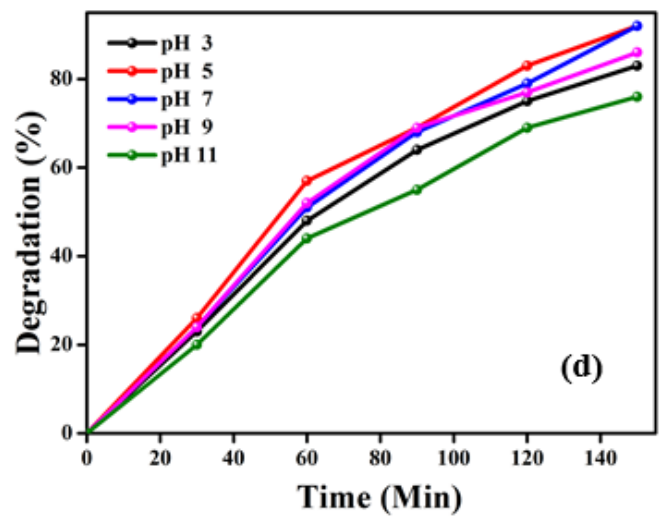
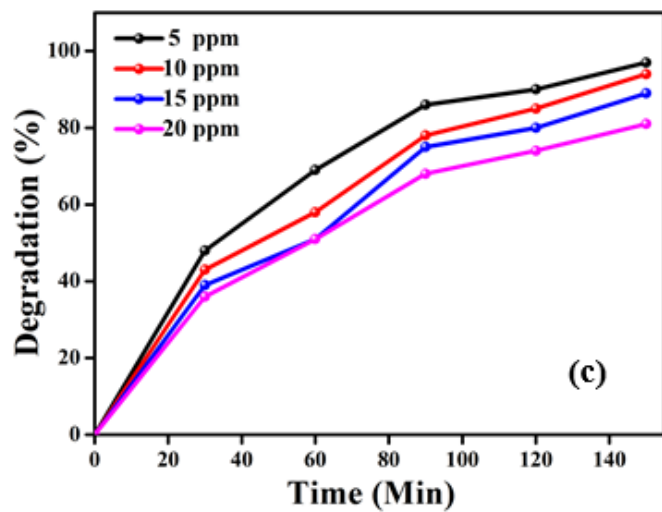
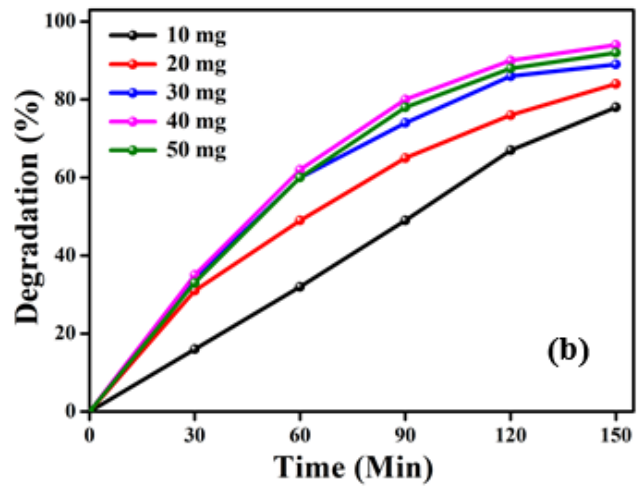
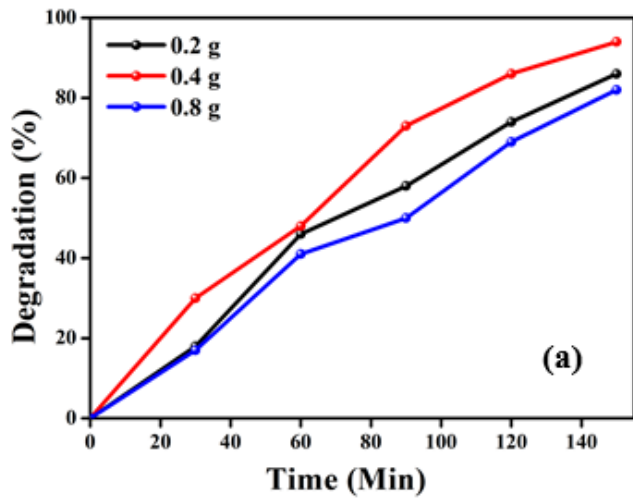


Figure 7

(a) Degradation plot of rose Bengal dye with 3 different fuel ratios of 3D-F-KT NPs (b) Photocatalytic activity at different dye concentrations using 0.4g catalyst(c) Photocatalytic activity of 5ppm RB dye with different catalytic load of KT NPs (d) Effect of pH on photocatalytic activity of 3D-F-KT NPs.

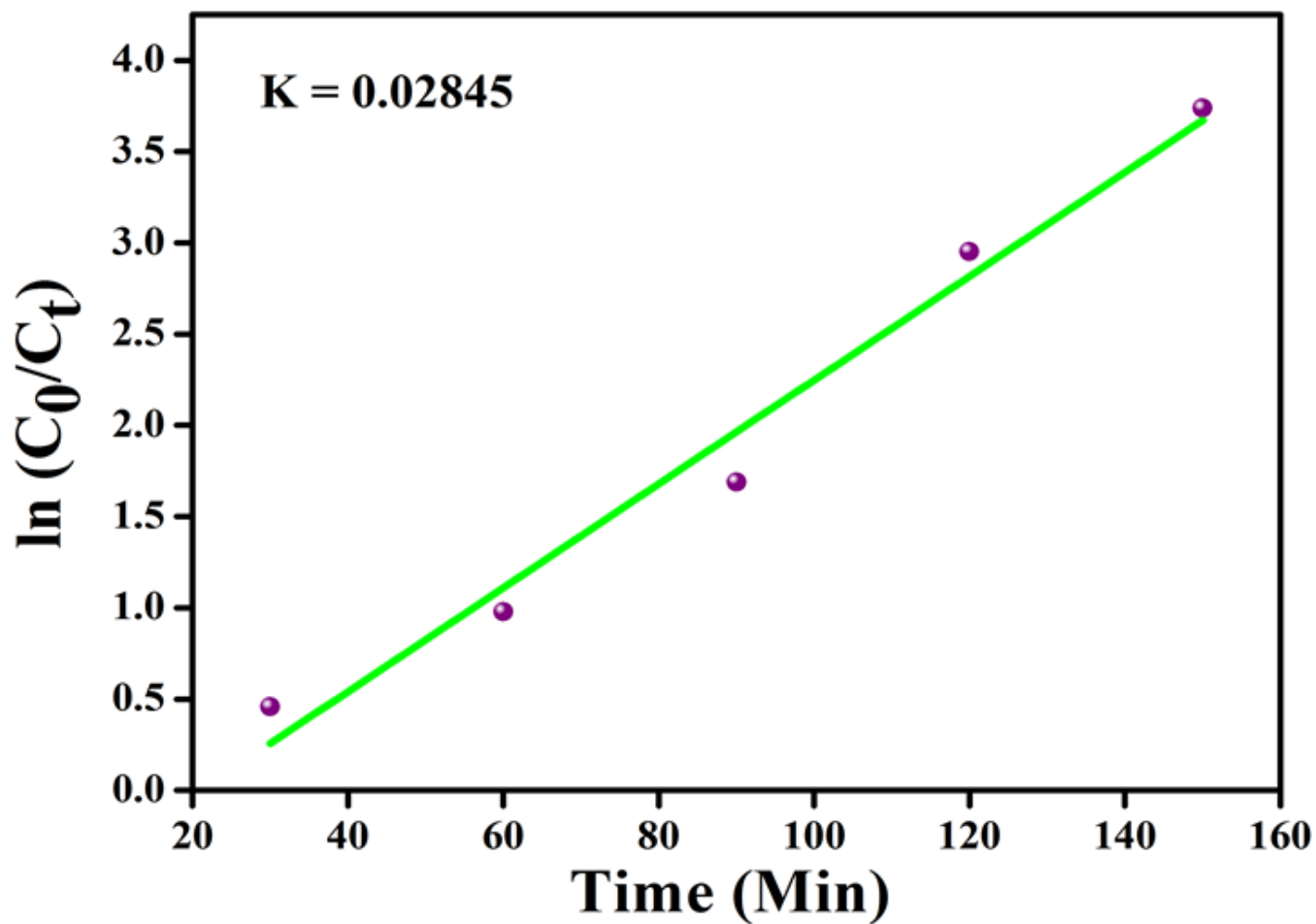


Figure 8

Rate constant plot of 3D-F-KT NPs (0.4g concentration of areca seed powder).

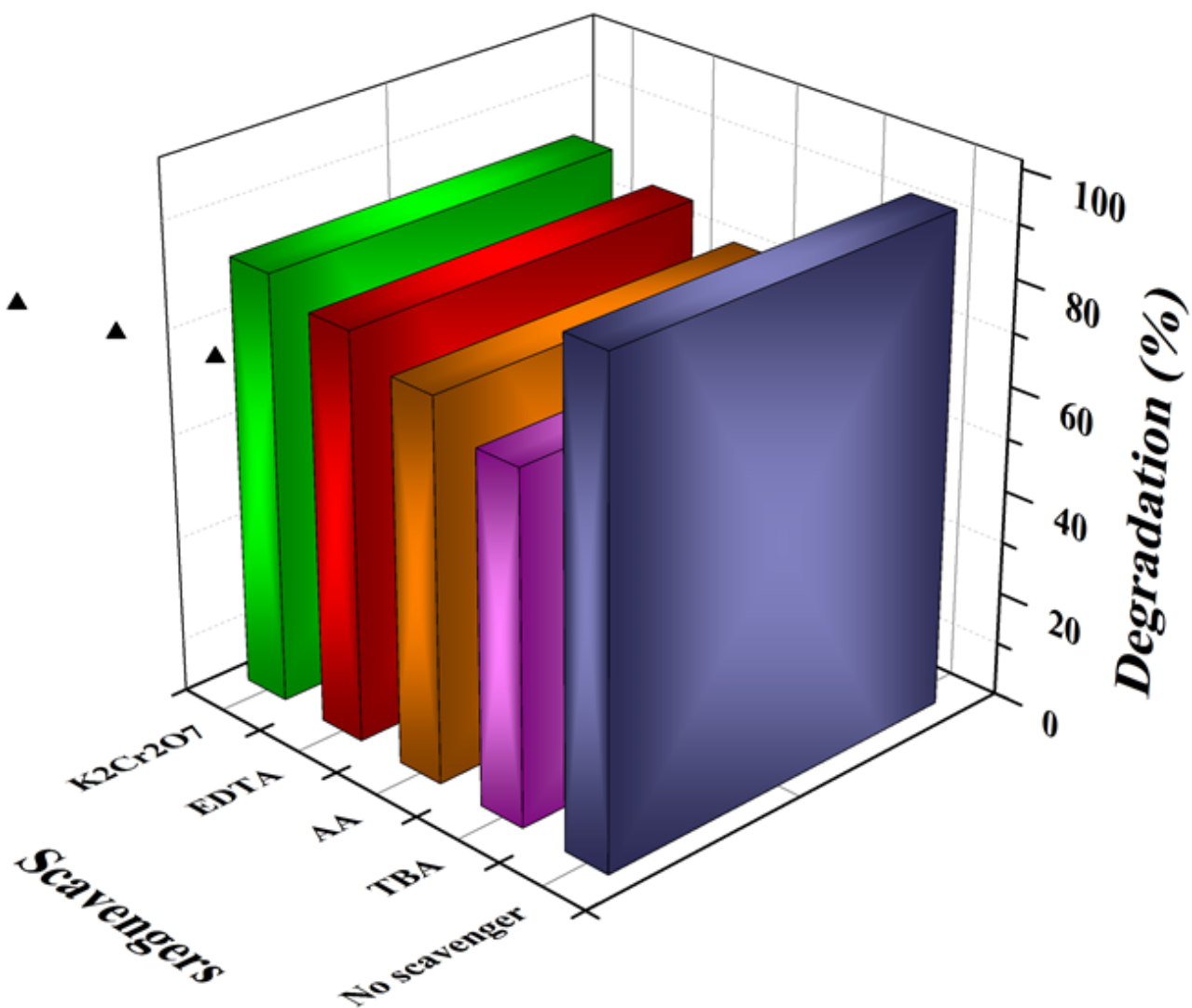


Figure 9

Effect of scavengers on photodegradation of RB by 3D-F-KT NPs (0.4g concentration of areca seed powder), showing major role of OH radical in degradation process under visible light irradiation.

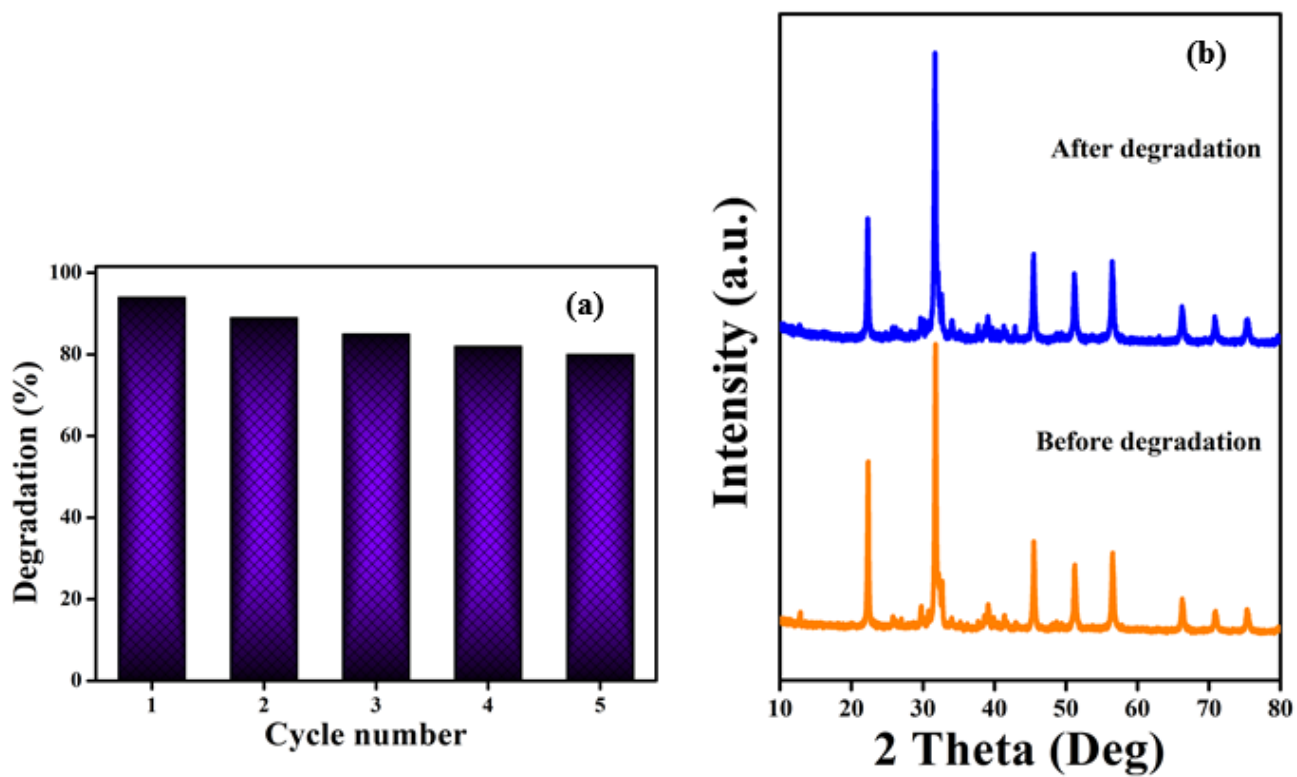


Figure 10

(a) Reusability over 5 cycles is achieved with excellent degradation efficiency and (b) XRD spectrum showing no change in peaks intensity -before and after degradation of 3D-F-KT (0.4g concentration of areca seed powder).

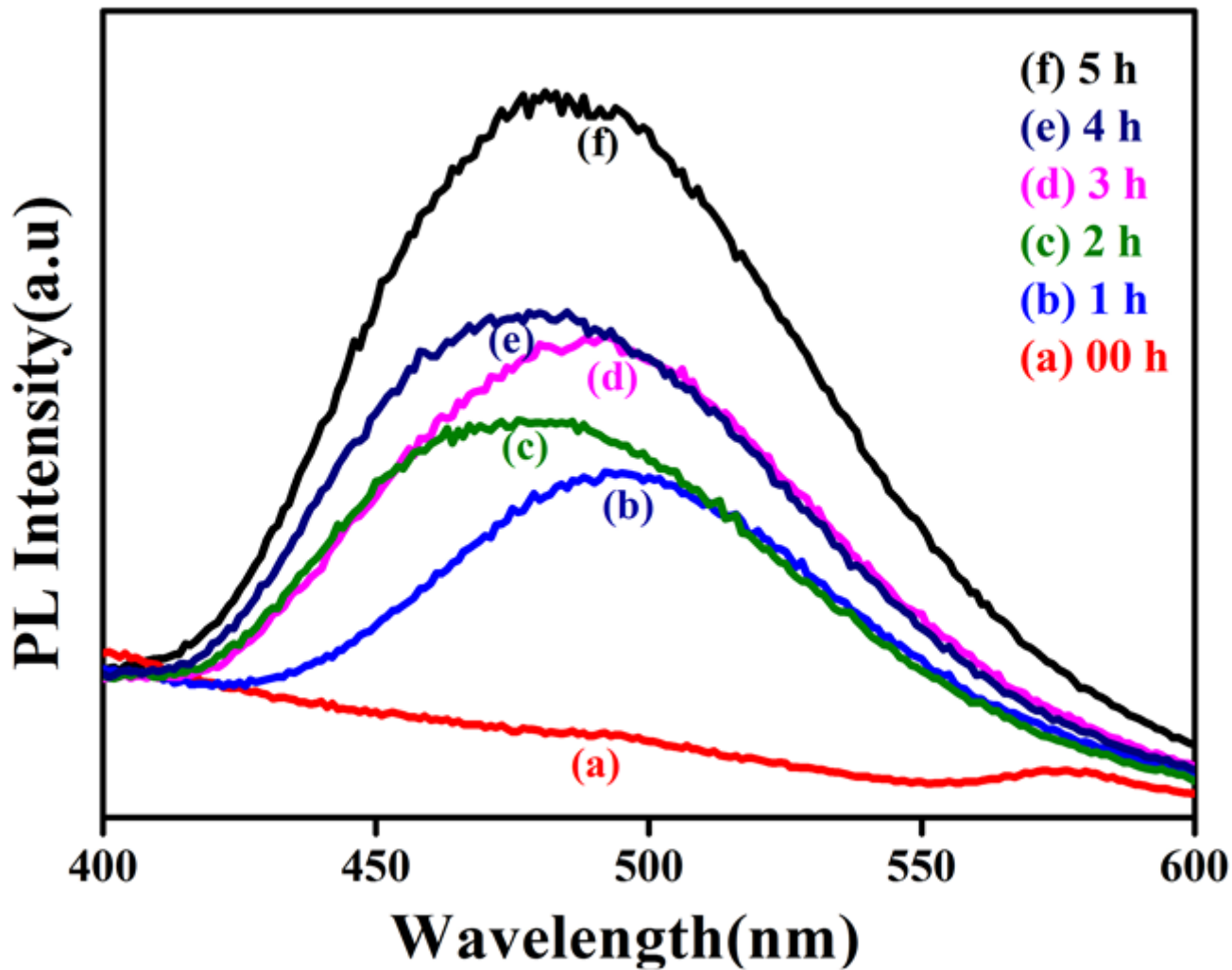


Figure 11

PL spectra showing the presence of large amount of OH radicals by forming 7-hydroxyl coumarin from coumarin upon increasing the time.

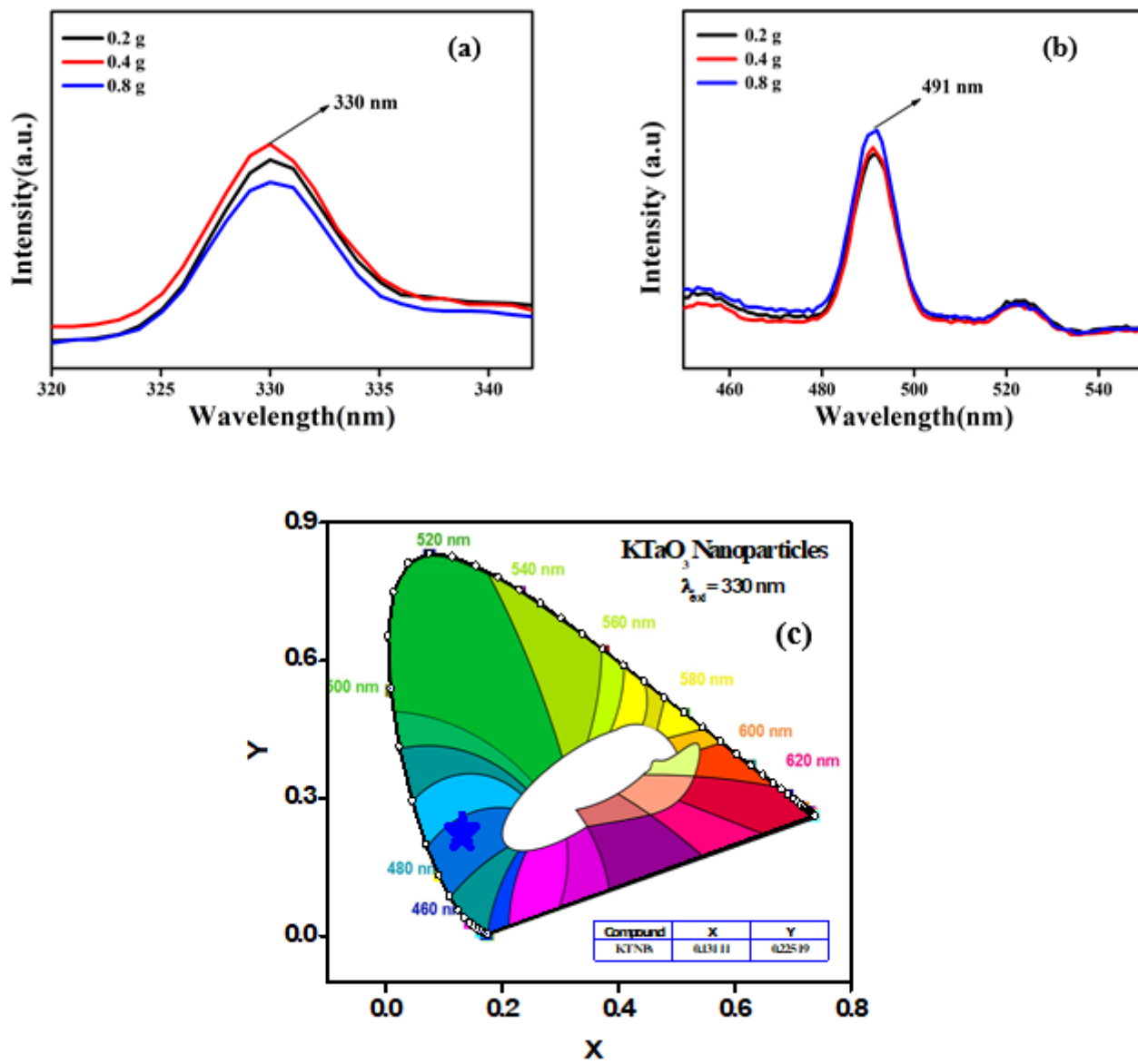


Figure 12

(a) PL excitation peak (b) emission peak (c) CIE diagram showing the emission of blue colour of 3D-F-KT NPs prepared by different concentrations of areca seed powder

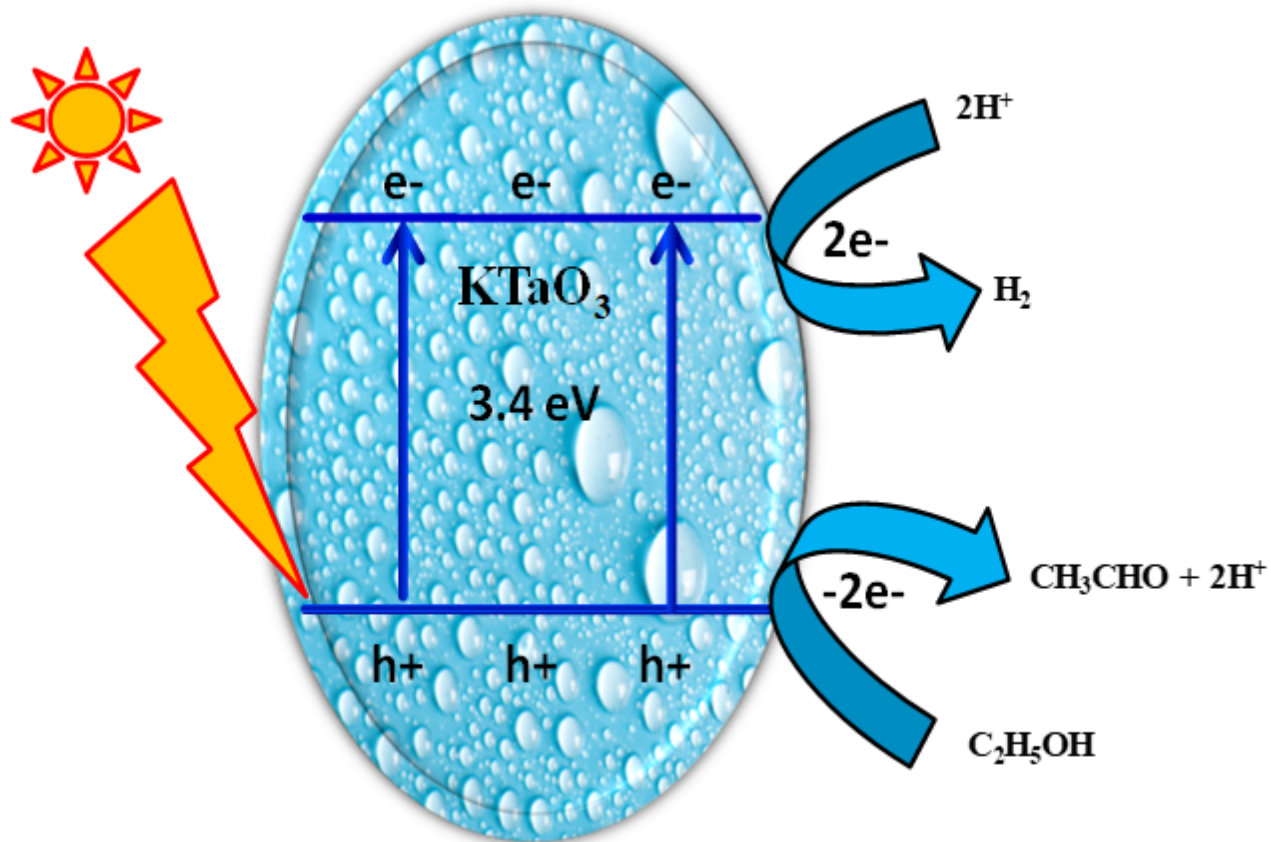


Figure 13

Schematic representation of photocatalytic reaction for the H_2 production under UV-visible light irradiation

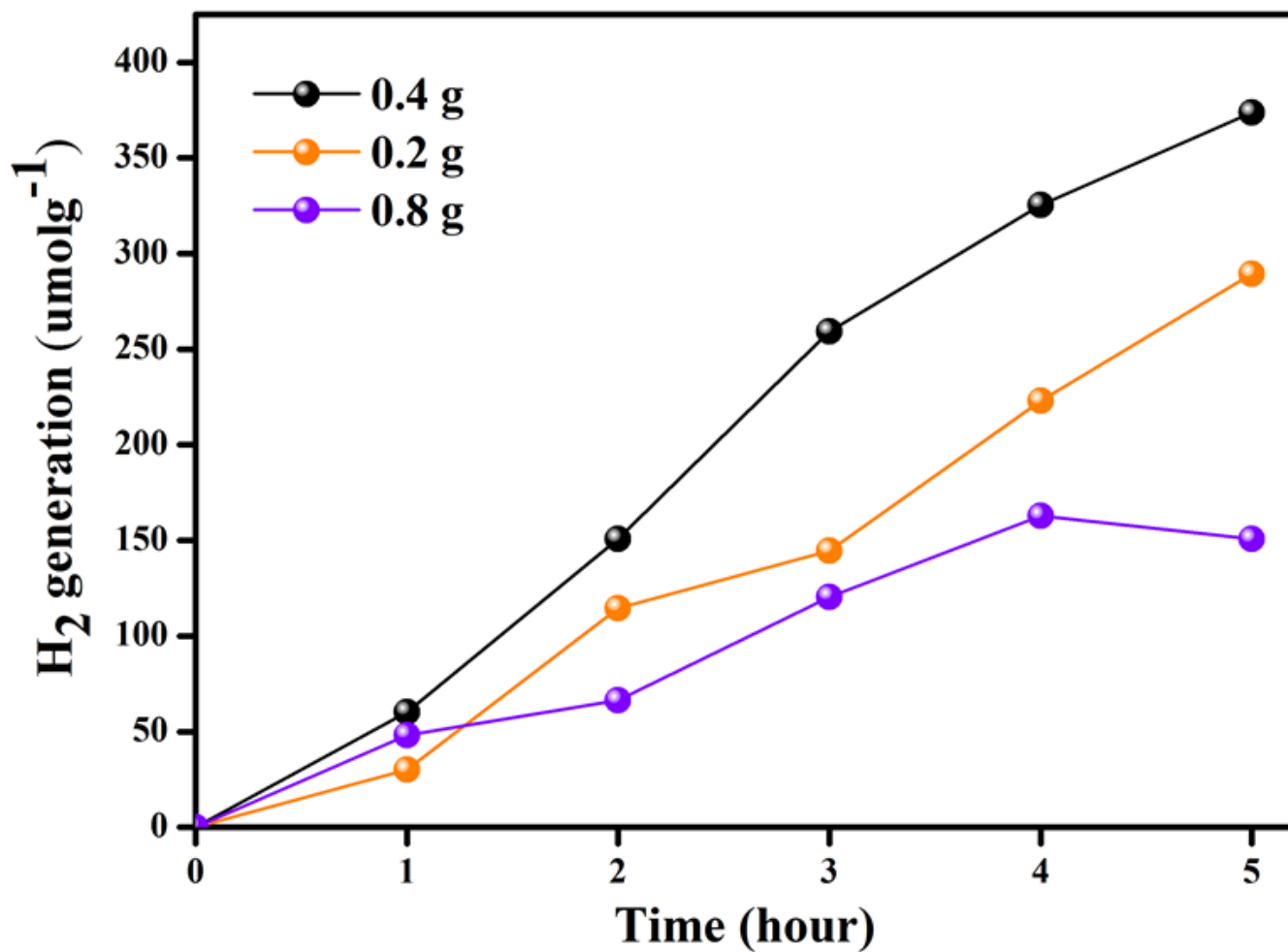


Figure 14

3D-F KT prepared by 0.4g concentration of areca seed powder shows higher H₂ generation than other 2 concentrations.

Supplementary Files

This is a list of supplementary files associated with this preprint. Click to download.

- [SCHEME1.png](#)